elastic strains associated with twin boundaries were introduced into the solid solution matrix, the segregation of Gd or Zn atoms, or both, into the strained sites led to reduced elastic strain energies associated with Gd or Zn atoms and twin boundaries. The DFT computations and continuum estimates both indicated that the ordered segregation of solute atoms in twin boundaries was driven by the minimization of the total energy (fig. S5) and elastic strain energy (table S4) in the system and did indeed reach equilibrium. These periodic solute segregation patterns can be considered as grain boundary "complexions" (4, 25, 26): They are thermodynamically stable only in twin boundaries.

We examined the effects of this phenomenon on the mobility of twin boundaries in and the deformation behavior of Mg alloys, finding that the ordered distribution of solute atoms exerted a stronger pinning effect on any further migration of the twin boundary than expected for individual solute atoms and, hence, a larger strengthening effect. Experimentally, we studied the pinning effect with two identical specimens of a Mg–Gd solid solution alloy. Both samples were unloaded immediately after compressed to 0.025 strain. After unloading, one specimen was compressed again to an accumulated strain of 0.045, whereas the other was annealed at 150°C for 3 hours and compressed again to an accumulated strain of 0.045. We observed twins in both samples after the first compression (Fig. 4, A and C). For the sample without annealing, we detected further growth of twins generated during the first compression (Fig. 4B, red arrow). The boundaries of most twins were noticeably expanded by the second compression. For the annealed specimen,

the size and shape of most preexisting twins remained almost unchanged (Fig. 4, C and D), but some new, small-sized twins also formed (Fig. 4D, red arrow). Analogous experiments on a Mg–0.4 atomic % Zn solid solution alloy yielded a similar but less thermally stable pinning effect (Fig. 4, E to H, and fig. S8).

The pinning effect on the mechanical properties of a binary Mg–Gd solid solution alloy is shown in Fig. 4I. Three identical samples were compression tested at room temperature. The first sample was loaded, unloaded, and immediately reloaded; we observed little strength change from the testing interruption. The second specimen was annealed at 150°C for 3 hours after unloading and before reloading, which led to an appreciable strengthening effect, rather than the weakening that would be expected according to conventional understanding. Before the first loading of the third specimen, it was given the same heat treatment, but this caused neither a weakening nor the strengthening that was observed in the second specimen.

The findings are expected to lead to new insights into the structure and chemistry of fully coherent twin boundaries in other hexagonal materials and cubic materials, as well as strategies for engineering the design of alloy compositions and thermomechanical processes in order to achieve desired formability and mechanical properties.

References and Notes

1. K. Lu, L. Lu, S. Suresh, *Science* **324**, 349 (2009).
2. K. Lu, L. Lu, *Scr. Mater.* **66**, 835 (2012).
3. L. Lu, Y. Shen, X. Chen, L. Qian, K. Lu, *Science* **304**, 422 (2004).
4. M. P. Harmer, *Science* **332**, 182 (2011).
5. V. Randle, *Acta Mater.* **52**, 4067 (2004).
6. T. M. Pollock, *Science* **328**, 986 (2010).
7. S. R. Agnew, J. F. Nie, *Scr. Mater.* **63**, 671 (2010).
8. J. W. Christian, S. Mahajan, *Prog. Mater. Sci.* **39**, 1 (1995).
9. Q. Yu et al., *Nano Lett.* **12**, 887 (2012).
10. B. Li, E. Ma, *Phys. Rev. Lett.* **103**, 035503 (2009).
11. B. Li, E. Ma, *Acta Mater.* **57**, 1734 (2009).
12. J. Wang, I. J. Beyerlein, J. P. Hirth, C. N. Tome, *Acta Mater.* **59**, 3990 (2011).
13. J. Wang, J. P. Hirth, C. N. Tome, *Acta Mater.* **57**, 5521 (2009).
14. K. Hantzsche et al., *Scr. Mater.* **63**, 725 (2010).
15. J. D. Robson, N. Stanford, M. R. Barnett, *Acta Mater.* **59**, 1945 (2011).
16. J. Ye, R. K. Mishra, A. K. Sachdev, A. M. Minor, *Scr. Mater.* **64**, 292 (2011).
17. L. Lu, X. Chen, X. Huang, K. Lu, *Science* **323**, 607 (2009).
18. X. Li, Y. Wei, L. Lu, K. Lu, H. Gao, *Nature* **464**, 877 (2010).
19. Q. Yu et al., *Nature* **463**, 335 (2010).
20. J. Luo, H. Cheng, K. M. Asl, C. J. Kiely, M. P. Harmer, *Science* **333**, 1730 (2011).
21. J. P. Buban et al., *Science* **311**, 212 (2006).
22. Z. Wang et al., *Nature* **479**, 380 (2011).
23. S. J. Pennycook, D. E. Jesson, *Acta Metall. Mater.* **40**, S149 (1992).
24. D. A. Muller, *Nat. Mater.* **8**, 263 (2009).
25. S. J. Dillon, M. Tang, W. C. Carter, M. P. Harmer, *Acta Mater.* **55**, 6208 (2007).
26. M. P. Harmer, *J. Am. Ceram. Soc.* **93**, 301 (2010).

Separation of Hexane Isomers in a Metal-Organic Framework with Triangular Channels

Zoey R. Herm,[1] Brian M. Wiers,[1] Jarad A. Mason,[1] Jasper M. van Baten,[2] Matthew R. Hudson,[3] Pawel Zajdel,[4] Craig M. Brown,[3,5] Norberto Masciocchi,[6] Rajamani Krishna,[2]* Jeffrey R. Long[1]*

Metal-organic frameworks can offer pore geometries that are not available in zeolites or other porous media, facilitating distinct types of shape-based molecular separations. Here, we report $Fe_2(BDP)_3$ (BDP^{2-} = 1,4-benzenedipyrazolate), a highly stable framework with triangular channels that effect the separation of hexane isomers according to the degree of branching. Consistent with the varying abilities of the isomers to wedge along the triangular corners of the structure, adsorption isotherms and calculated isosteric heats indicate an adsorption selectivity order of *n*-hexane > 2-methylpentane > 3-methylpentane > 2,3-dimethylbutane ≈ 2,2-dimethylbutane. A breakthrough experiment performed at 160°C with an equimolar mixture of all five molecules confirms that the dibranched isomers elute first from a bed packed with $Fe_2(BDP)_3$, followed by the monobranched isomers and finally linear *n*-hexane. Configurational-bias Monte Carlo simulations confirm the origins of the molecular separation.

Metal-organic frameworks constitute a large family of microporous solids exhibiting high surface areas, tunable pore dimensions, and adjustable surface functionality (1–3). Consequently, their performance is beginning to rival traditional solid adsorbents, such as zeolites and activated carbons, for some key gas-storage (4–7) and molecular-separation (8–12) applications. With regard to the latter, the possibility of creating pore characteristics that cannot readily be achieved in zeolites or carbons expands the opportunities for molecular recognition. In the presence of the right surface environment, separations currently carried out inefficiently could potentially be performed with a substantially reduced energy cost (13). The efficient separation of alkane isomers by adsorption is especially challenging because the molecules are chemically inert and have similar polarizabilities (14), leaving shape as the main handle available for their differentiation. This separation is critical to

[1]Department of Chemistry, University of California, Berkeley, CA 94720, USA. [2]Van't Hoff Institute for Molecular Sciences, University of Amsterdam, Science Park 904, 1098 XH Amsterdam, Netherlands. [3]Center for Neutron Research, National Institute of Standards and Technology, Gaithersburg, MD 20899, USA. [4]Institute of Physics, University of Silesia, ul. Uniwersytecka 4, 40-007 Katowice, Poland. [5]Chemical and Biomolecular Engineering, University of Delaware, Newark, DE 19716, USA. [6]Dipartimento di Scienza e Alta Tecnologia, Università dell'Insubria, via Valleggio 11, I-22100 Como, Italy.

*Corresponding author. E-mail: r.krishna@uva.nl (R.K.); jrlong@berkeley.edu (J.R.L.)

the production of gasoline, which is composed of ~10% pentanes and hexanes (15). Herein, we report a metal-organic framework featuring sharply angled pore walls of a type not encountered in zeolites and capable of fractionating alkane isomers according to the degree of branching.

Hexanes of formula C_6H_{14} are generated at enormous scale through a catalytic isomerization reaction that results in a thermodynamically controlled product stream composed of 10 to 30% of each of the five different isomers (15). The value of a particular isomer as a component in the gasoline pool is related to its research octane number (RON) and is highest for the dibranched hexanes 2,3-dimethylbutane and 2,2-dimethylbutane, which have values of 105 and 94, respectively. The RONs for the monobranched isomers 2-methylpentane and 3-methylpentane are substantially lower, at 74 and 75, respectively, whereas the value for linear n-hexane is only 30. To achieve higher octane number blends, current processes sieve n-hexane by using zeolites, generating a mixture of the other four isomers with a final RON of nearly 83 while returning n-hexane to the isomerization reactor (15–17). Additionally, some separation processes achieve higher-grade mixtures by subsequently distilling the monobranched isomers away from the valuable dimethylbutane products. Currently, about two million barrels of pentanes and hexanes are processed daily (15).

An improved hexane-separation process would selectively isolate the most valuable products, 2,3-dimethylbutane and 2,2-dimethylbutane, while returning the less valuable monobranched isomers to the isomerization reactor along with n-hexane (Fig. 1) (18). Further, it would potentially benefit public health, because it could reduce the usage of toxic aromatics, which are currently added to boost the octane number of gasoline (19). Performing this separation at or near the isomerization temperature would save a great deal of energy in the production of high-quality gasoline. Numerous attempts have been made to identify solid adsorbents capable of effecting an efficient separation of hexane isomers according to octane number, including zeolites (20, 21), silicas (22), and, very recently, metal-organic frameworks

(18, 23, 24). Although zeolite BETA facilitates the separation of 2,2-dimethylbutane from the monobranched isomers and some 2,3-dimethylbutane (the highest value isomer) elutes with it, these results are only seen at 0.01 bar and are therefore not useful for a separation (21). The many studies that have examined the adsorption or separation of some hexane isomers generally do not include the crucially important separation of both 2,2-dimethylbutane and 2,3-dimethylbutane from the monobranched and linear isomers.

In comparing the structures of zeolites to those possible in metal-organic frameworks, a prominent distinction lies in the angles that can be obtained for the internal pore walls. Whereas the pore contours defined by a zeolite scaffolding are necessarily obtuse, owing to the O-Si-O and Si-O-Si angles of ~109° and >130°, respectively (25), the higher coordination numbers possible for the metal nodes within a metal-organic framework can give rise to flat pore surfaces that intersect at acute angles. An extreme example of this is apparent in the structure of the new metal-organic framework $Fe_2(BDP)_3$ (Fig. 2), which we obtained as a black microcrystalline solid upon reaction of $Fe(acetylacetonate)_3$ and 1,4-benzenedipyrazole (H_2BDP) in N,N-dimethylformamide (26). Here, octahedral iron(III) centers are linked via μ^2-pyrazolate units to form chains running along one crystal axis (Fig. 2C), where both nitrogens on one ring bind to different iron atoms. The rigid, nearly planar BDP^{2-} ligands (Fig. 2B) define a channel structure featuring sharply angled crevices running along the triangle corners. The chains of octahedral iron(III) centers form the vertices of these triangles. One can readily envision how these crevices might provide strong van der Waals contacts for linear alkanes, whereas branched alkanes would protrude into the pores. The framework of $Fe_2(BDP)_3$ is directly analogous to the carboxylate-linked structure of $Sc_2(BDC)_3$ (BDC^{2-} = 1,4-benzenedicarboxylate) (27) but with a larger metal···metal triangle-edge length of 13.25(2) Å as a result of the longer BDP^{2-} linker. The structure is also related to that of Co(BDP), wherein chains of tetrahedral cobalt(II) centers lead instead to square channels (28).

The strong iron(III)-pyrazolate bonds and highly connected architecture of $Fe_2(BDP)_3$ lend it exceptional chemical and thermal stability. The material can be boiled in aqueous solutions at pH = 2 to 10 for 2 weeks (fig. S1) or heated in air to at least 280°C (fig. S2) without losing crystallinity. Heating the solvated, as-synthesized form of $Fe_2(BDP)_3$ at 180°C under dynamic vacuum afforded a completely activated, microporous form of the compound exhibiting a Brunauer-Emmett-Teller surface area of 1230 m^2/g.

Pure-component equilibrium adsorption isotherms for the five different hexane isomers were measured for $Fe_2(BDP)_3$ at temperatures of 130°, 160°, and 200°C (Fig. 3), within the range of 100° to 200°C relevant to the industrial separation (15). In contrast to zeolite 5A, which operates as a sieve for separating n-hexane, the dimensions of the channels in the evacuated structure of $Fe_2(BDP)_3$ are large enough to accommodate all five hexane isomers. At 130°C, the isotherm data rise with varying degrees of steepness until reaching saturation. The decreasing degrees of steepness in the isotherms for linear versus monobranched versus dibranched isomers indicate a corresponding decrease in the adsorption strength. At 200°C, the isotherms rise considerably less steeply and do not reach saturation. At 160°C, n-hexane and the monobranched isomers exhibit the behavior expected of an interpolation between the 130° and 200°C isotherms: Saturation capacity is reached or nearly reached, but at pressures higher than those required at 130°C. At about 100 mbar and 200°C, $Fe_2(BDP)_3$ adsorbs 60% more n-hexane by volume and 100% more by weight than zeolite 5A (29). This enhancement, together with the adsorption selectivity discussed further below, renders $Fe_2(BDP)_3$ a more efficient adsorbent than zeolite 5A for the n-hexane separation presently carried out in industry.

At 160°C, the two dibranched hexane isomers display stepwise adsorption with an inflection point near 100 mbar. The stepwise uptake of alkanes has been observed previously with cyclohexane (30) and n-hexane (31) adsorption, and can be explained with entropic arguments, as supported by calorimetric data (32). Here, the inflection point occurs near 0.5 moles of guest per mole of $Fe_2(BDP)_3$. As supported by the simulations discussed below, rearrangement occurs at this loading based on packing around the structural ridge that is created along the triangular channel by two adjacent $Fe_2(BDP)_3$ subunits (Fig. 2D). This behavior is not evident at 200°C because a loading of 0.5 mole is not attained under the conditions measured. The step is not as prominent at 130°C for two reasons: (i) The entropic component of the Gibbs free energy is smaller at lower temperatures, and (ii) the steepness of the isotherm obscures the feature.

Complementary to the ordered adsorption of dibranched isomers, neutron diffraction data demonstrate the lack of a preferred arrangement of n-hexane molecules within the pores of $Fe_2(BDP)_3$. Diffraction patterns were collected at 10 K on microcrystalline powders loaded with 0.5 and 1.0
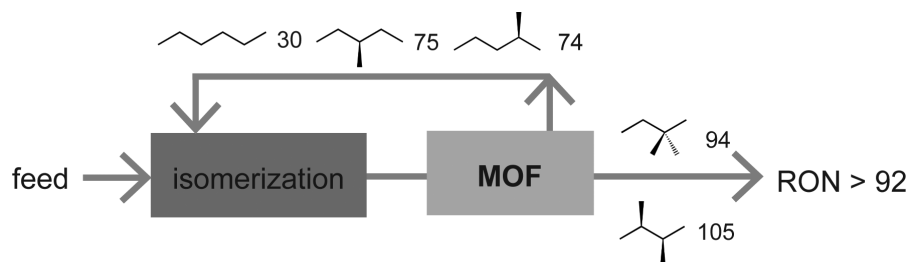

Fig. 1. Illustration of the proposed future hexane isomer separation processes. The individual RON of each isomer and the average RON of the final product are included. Current technology uses the small cross-sectional area of n-hexane and a zeolite-sieving process to remove this low-RON isomer from the mixture and return it to the isomerization reactor. In some cases, distillation is then used to further augment the RON of the final product. Given the adsorption selectivity that can be attained within a metal-organic framework (MOF) as demonstrated here for $Fe_2(BDP)_3$, it may now be viable to separate only the two most valuable, dibranched isomers from the other three.

molar equivalents of perdeuterated *n*-hexane. Attempts to refine the position of the *n*-hexane molecules in both samples were thoroughly exhausted by using several different refinement approaches, suggesting that there is unlikely any correlation between the positions of guests adsorbed in each pore.

In addition to entropic differences, the enthalpies of adsorption among the five hexane isomers in $Fe_2(BDP)_3$ are dependent on the degree
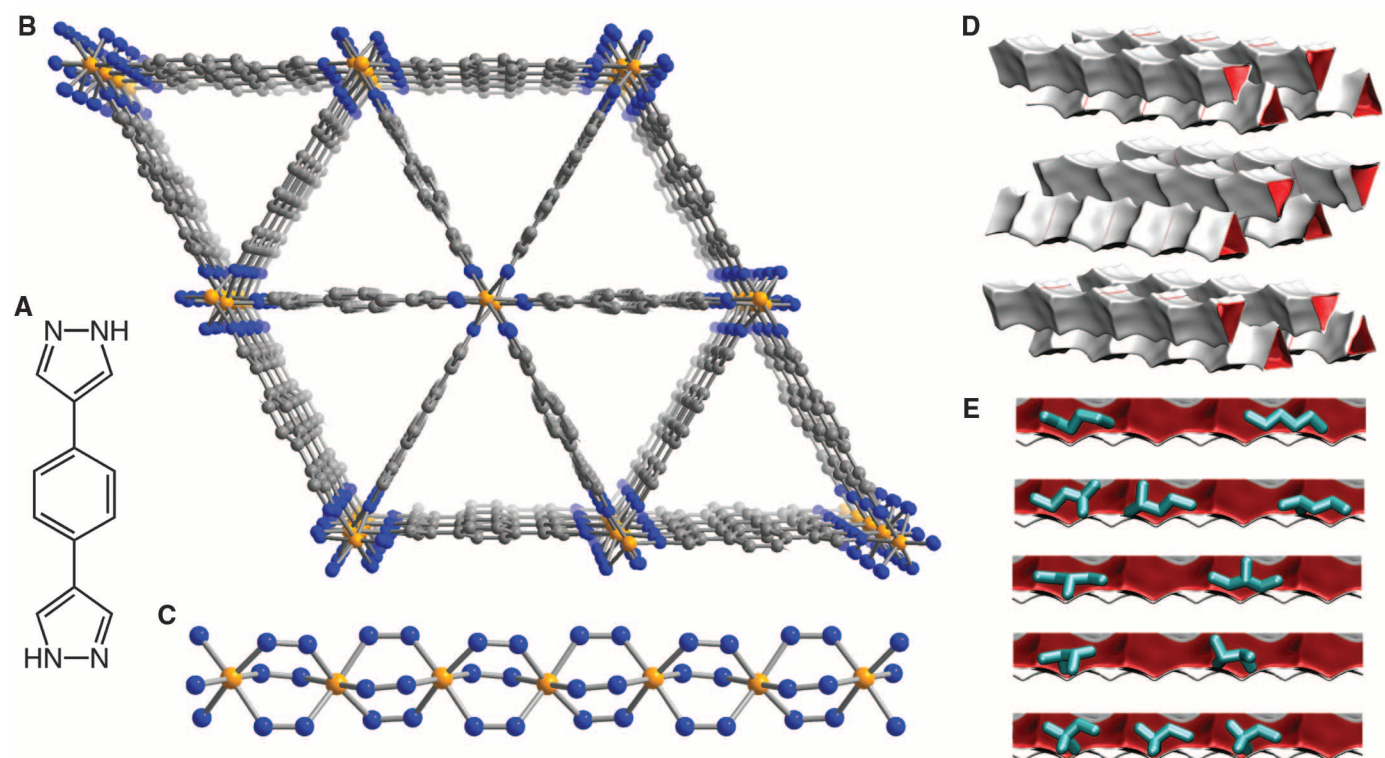
Fig. 2. Chemical structures. Depiction of the bridging ligand precursor H_2BDP (**A**) and portions of the structure of $Fe_2(BDP)_3$ as determined by analysis of powder x-ray diffraction data. Orange, blue, and gray spheres represent Fe, N, and C atoms, respectively; H atoms are omitted for clarity. (**B**) The view along the [001] direction in the orthorhombic crystal structure (space group *Fddd*). (**C**) A perpendicular view of the one-dimensional chains of pyrazolate-bridged Fe^{III} octahedra, excluding C and H atoms. Selected interatomic distances and angles are as follows: for Fe-N1x, 1.98 Å; Fe-N2, 2.04 Å; Fe-N1, 1.94 Å; Fe···Fe (vertex to vertex), 13.25 Å; Fe-Fe (nearest neighbor), 3.85 Å; N1x-Fe-N2, 7°; N1x-Fe-N2′, 92.5°; N1x-Fe-N1, 81.2°; N1x-Fe-N1′, 88.9°; N1-Fe-N2, 91.6°; Fe-N1x-N1x, 123.1°; Fe-N2-N1, 115.6°; Fe-N1-N2, 131.0°. Typical estimated standard deviations are 0.01 Å for bond distances and 0.1° for bond angles. (**D**) The van der Waals surfaces associated with the corrugated triangular channels running through the structure. (**E**) Snapshots of the hexane isomers within the channels of $Fe_2(BDP)_3$ for a loading of four molecules per unit cell at 160°C, as observed in CBMC simulations.

Fig. 3. Pure-component equilibrium adsorption isotherms. Gas adsorption isotherms for (**A**) *n*-hexane, (**B**) 2-methylpentane, (**C**) 3-methylpentane, (**D**) 2,3-dimethylbutane, and (**E**) 2,2-dimethylbutane in $Fe_2(BDP)_3$ at 130°C (squares), 160°C (circles), and 200°C (diamonds). Lines represent dual-site Langmuir-Freundlich fits to these data (table S2). Isosteric heats of adsorption (Q_{st}) calculated from these isotherm data are plotted in (**F**) as a function of loading.
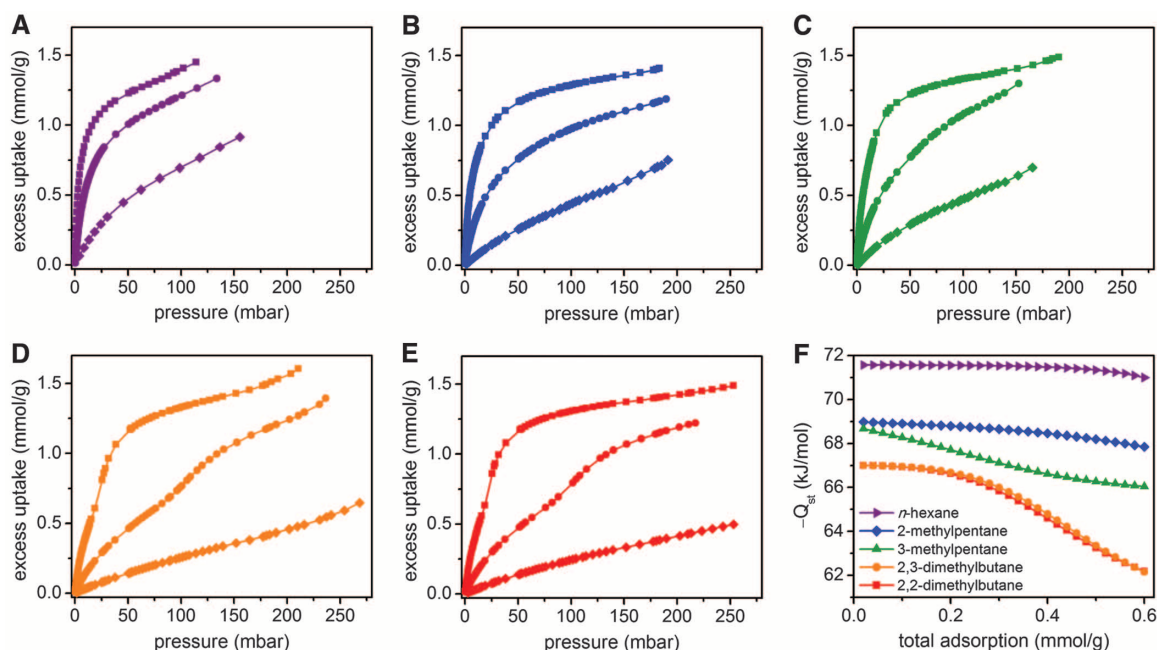
of branching as well. Isosteric heats of adsorption (Fig. 3F) were calculated by differentiation of the temperature-independent, combined dual-site Langmuir-Freundlich fits to the isotherm data obtained at 130°, 160°, and 200°C. In order to report enthalpy values obtained without extrapolation, the results are only plotted up to the highest loading attained at the highest temperature. The linear n-hexane isomer has the strongest interaction with the framework, because a greater fraction of its surface can interact with the triangular channel pore surface than the other isomers. Comparing methylpentane isomers, the zero-coverage isosteric heat is initially very similar, but as more guests enter the pores, the strength of interaction of the two isomers diverges. Here, the higher flexibility of the 2-methylpentane chain apparently allows a stronger adsorbate-adsorbent interaction to be maintained at higher loadings. The more compact dimethylbutane isomers are not flexible enough to maximize van der Waals interactions with the pore surfaces and have the lowest enthalpies at all loadings. This trend in selectivity has occasionally been observed at very low loadings in zeolites as a result of different isomers residing in different parts of a heterogeneous pore structure (33), but at more substantial loadings it disappears. In contrast, for $Fe_2(BDP)_3$, the isomers are all interacting with the same, relatively homogeneous surface differently. This trend has also been observed in other metal-organic frameworks for a selected subset of hexane isomers (23, 34) but never for all five isomers.

Taken together, the trends in the enthalpy and entropy of adsorption for the five hexane isomers conspire to generate a free energy hierarchy of linear < monobranched < dibranched isomer adsorption. The linear isomers bind more strongly and additionally do not require substantial reorganization at loadings above 0.5 molecules per unit cell. Although separate enthalpy (35) and entropy (36) trends of this type have been established previously, the combined contributions of both within $Fe_2(BDP)_3$ offers exceptional potential for separating the valuable dibranched hexanes from the other isomers.

The hexane isomer separation ability of $Fe_2(BDP)_3$ was evaluated with a breakthrough experiment in which an equimolar mixture of all five isomers in N_2 was passed over a bed of the material heated at 160°C. As shown in Fig. 4A, pure 2,2-dimethylbutane eluted from the bed, followed by 2,3-dimethylbutane. These dibranched isomers are the most desirable, owing to their high RON values. Monobranched 2-methylpentane eluted subsequently, immediately followed by 3-methylpentane and then, much later, linear n-hexane. The RON of the product mixture leaving the column is also plotted in Fig. 4A, simplified as a weighted average of the RONs of each component (16). During the beginning of the breakthrough experiment, the RON of the eluted mixture rises to greater than 90, significantly higher than the value of 83 that is typical for industrially refined hexane blends (15).

The shape of the breakthrough curve for each isomer is informative with regard to the separation (18). The steepness of the dimethylbutane breakthrough events suggests that the separations for these isomers result from essentially equilibrium processes and are not diffusion controlled. As shown in Fig. 3F, the enthalpy of adsorption for the two dimethylbutane isomers is essentially identical up to a loading of 0.6 mmol/g. If diffusion is not the primary cause of the separation and the material is saturated at the breakthrough event, the strength of adsorption of these isomers presumably diverges at higher loadings, with 2,3-dimethylbutane adsorbing more strongly. The methylpentanes and n-hexane display more gradual breakthrough events, suggesting that diffusion is a contributory factor in their elution dynamics.

Pulse chromatography simulations (26) were performed to further probe the separation properties of $Fe_2(BDP)_3$. The results (Fig. 4B) indicate that the material can separate a mixture of hexane isomers into three fractions, consisting of the two dimethylbutane isomers, the two methylpentane isomers, and, finally, pure n-hexane. These three fractions could potentially serve independent purposes: The dibranched isomers would be added

to gasoline, the n-hexane would be reintroduced to the isomerization reactor as it is presently, and the monobranched isomers could be returned to the isomerization reactor at a downstream location, allowing for better conversion (fig. S3). It is expected that such a staged recycling scheme could significantly boost the efficiency of the isomerization process.

Configurational-bias Monte Carlo (CBMC) simulations illustrate and support the mechanism of hexane isomer fractionation in $Fe_2(BDP)_3$. The methodology used has been described in detail (37), and the Lennard-Jones parameters used for the atoms of the framework are specified in table S1. The results are presented in Fig. 2E as snapshots of the locations and conformations of hexane isomers adsorbed within the triangular channels of the structure. The snapshots are obtained from arbitrary channel segments, and so, although the simulated loading of four molecules per unit cell is the same overall for each isomer, the number of molecules in each channel differs among the images. The regularity of the 2,3-dimethylbutane and 2,2-dimethylbutane positions supports the hypothesis that these molecules have a preferred arrangement, one that requires energy input to overcome. The snapshots also validate the enthalpic argument that van der Waals overlap decreases with the degree of branching, a hypothesis previously put forth to explain the trends in the diffusion rates for pentane isomers in zeolite NaY (38). Generally, the hexane backbones align along the vertices of the triangular channels, which provide the maximum surface area for dispersion interactions. Figs. S4 and S5 include more arbitrary channel segments to provide more support for these arguments. From the observed conformations, it is evident that the number of carbon atoms that can effectively interact with the pore wall decreases with the degree of branching. The dimethylbutane isomers are more compact and have the weakest van der Waals interactions with the framework surface.

Comparisons with published data and further CBMC simulations demonstrate the unique efficacy of $Fe_2(BDP)_3$ in separating hexane isomers

Fig. 4. Separation of an equimolar mixture of 2,2-dimethylbutane (red), 2,3-dimethylbutane (orange), 3-methylpentane (green), 2-methylpentane (blue), and n-hexane (purple) running through a packed bed of $Fe_2(BDP)_3$ at 160°C. (**A**) Experimental breakthrough data, together with the RON calculated for the eluted mixture at 1 bar. (**B**) The pulsed chromatogram calculated on the basis of the isotherm data presented in Fig. 3.
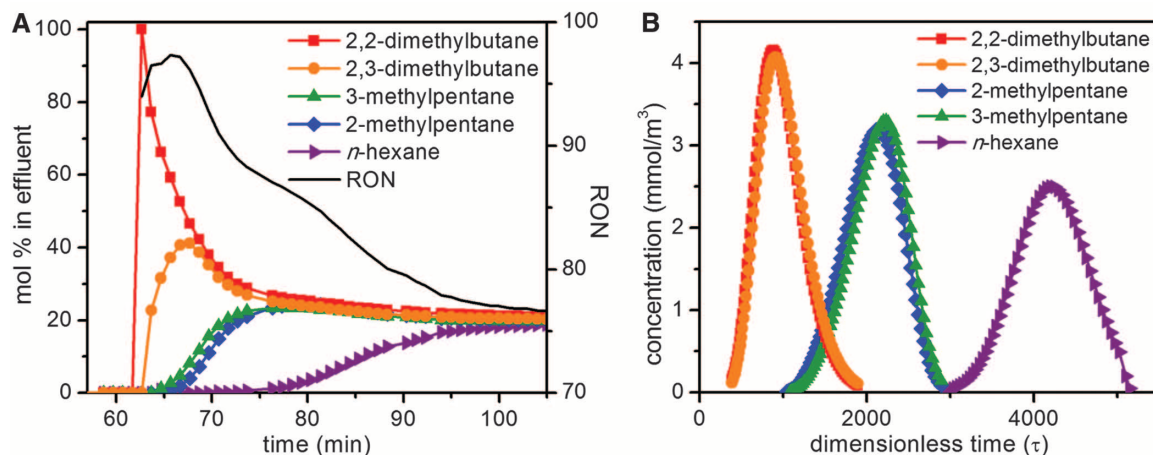
according to the degree of branching. A detailed comparison of its performance relative to zeolites and other metal-organic frameworks is provided in section 2.4 of the supplementary materials. A realistic comparison, of relevance to industrial operations, is obtained by comparing the number of moles of 92 RON product that can be obtained per liter of adsorbent in a packed bed adsorber, taking account of diffusional limitations. These comparisons show that for $Fe_2(BDP)_3$ the 92 RON productivity is 0.54 mol/l, whereas the values obtained for other adsorbents are consistently lower.

Very recently, a series of carboxylate-linked metal-organic frameworks with triangular channels was reported (39). Although these could potentially provide surrogates or even more efficient replacements for $Fe_2(BDP)_3$, our CMBC calculations suggest that the size of the channels in $Fe_2(BDP)_3$ is nearly optimal for a hexane isomer separation, as described in detail in section 2.4.14 of the supplementary materials. Narrower triangular channels cannot accommodate all five isomers, whereas wider channels do not maximize the differences in van der Waals contacts.

CBMC simulations indicate that $Fe_2(BDP)_3$ is similarly suitable for separating pentane and heptane isomers according to the degree of branching. For pentane isomers, the results indicate the hierarchy of adsorption strengths as n-pentane > 2-methylbutane > neopentane (fig. S6A); for heptanes, they follow the order n-heptane > 2-methylhexane ≈ 3-methylhexane > 2,2-dimethylpentane ≈ 2,3-dimethylpentane (fig. S6D). Accordingly, pulse chromatography simulations reveal the extraordinary ability of $Fe_2(BDP)_3$ to separate the di-branched alkanes with high RON values from a mixture of pentane, hexane, and heptane isomers (fig. S7).

References and Notes

1. M. Eddaoudi et al., Science 295, 469 (2002).
2. S. Kitagawa, R. Kitaura, S.-i. Noro, Angew. Chem. Int. Ed. 43, 2334 (2004).
3. G. Férey, Chem. Soc. Rev. 37, 191 (2008).
4. X. Lin, N. R. Champness, M. Schröder, Top. Curr. Chem. 293, 35 (2010).
5. M. P. Suh, H. J. Park, T. K. Prasad, D.-W. Lim, Chem. Rev. 112, 782 (2012).
6. D. Liu et al., Chem. Sci. 3, 3032 (2012).
7. T. A. Makal, J.-R. Li, W. Lu, H.-C. Zhou, Chem. Soc. Rev. 41, 7761 (2012).
8. Z. Bao et al., Langmuir 27, 13554 (2011).
9. Y.-S. Bae et al., Angew. Chem. Int. Ed. 51, 1857 (2012).
10. E. D. Bloch et al., Science 335, 1606 (2012).
11. K. Sumida et al., Chem. Rev. 112, 724 (2012).
12. J.-R. Li, J. Sculley, H.-C. Zhou, Chem. Rev. 112, 869 (2012).
13. A. U. Czaja, N. Trukhan, U. Müller, Chem. Soc. Rev. 38, 1284 (2009).
14. D. H. Desty, W. T. Swanton, J. Phys. Chem. 65, 766 (1961).
15. R. A. Myers, Ed., Handbook of Petroleum Refining Processes (McGraw-Hill, New York, 2004).
16. R. Clavier, Ed., Wiley Critical Content: Petroleum Technology (Wiley-Interscience, Hoboken, NJ, 2007).
17. R. V. Jasra, S. G. T. Bhat, Sep. Sci. Technol. 23, 945 (1988).
18. D. Peralta, G. Chaplais, A. Simon-Masseron, K. Barthelet, G. D. Pirngruber, Ind. Eng. Chem. Res. 51, 4692 (2012).
19. F. Nadim, P. Zack, G. E. Hoag, S. Liu, Energy Policy 29, 1 (2001).
20. R. Krishna, B. Smit, S. Calero, Chem. Soc. Rev. 31, 185 (2002).
21. P. S. Bárcia, J. A. C. Silva, A. E. Rodrigues, Am. Inst. Chem. Eng. J. 53, 1970 (2007).
22. A. Silvestre-Albero et al., Langmuir 25, 939 (2009).
23. V. Finsy et al., Phys. Chem. Chem. Phys. 11, 3515 (2009).
24. P. S. Bárcia et al., Microporous Mesoporous Mater. 139, 67 (2011).
25. R. F. Lobo, in Handbook of Zeolite Science and Technology, S. M. Auerbach, K. A. Carrado, P. K. Dutta, Eds. (Marcel Dekker, New York, 2003), chap. 3.
26. Information on materials and methods is available as supplementary materials on Science Online.
27. S. R. Miller et al., Chem. Commun. 2005, 3850 (2005).
28. H. J. Choi, M. Dincă, J. R. Long, J. Am. Chem. Soc. 130, 7848 (2008).
29. J. A. C. Silva, A. E. Rodrigues, Ind. Eng. Chem. Res. 38, 2434 (1999).
30. K. Li et al., Chem. Commun. 2008, 6123 (2008).
31. B. Smit, T. L. M. Maesen, Nature 374, 42 (1995).
32. A. F. P. Ferreira, M. C. Mittelmeijer-Hazeleger, A. Bliek, J. A. Moulijn, Microporous Mesoporous Mater. 111, 171 (2008).
33. P. S. Bárcia, J. A. C. Silva, A. E. Rodrigues, Ind. Eng. Chem. Res. 45, 4316 (2006).
34. N. Chang, Z.-Y. Gu, X.-P. Yan, J. Am. Chem. Soc. 132, 13645 (2010).
35. P. S. Bárcia, J. A. C. Silva, A. E. Rodrigues, Microporous Mesoporous Mater. 79, 145 (2005).
36. T. J. H. Vlugt, R. Krishna, B. Smit, J. Phys. Chem. B 103, 1102 (1999).
37. D. Dubbeldam, R. Krishna, S. Calero, A. Ö. Yazaydin, Angew. Chem. Int. Ed. 51, 11867 (2012).
38. S. Y. Bhide, S. Yashonath, Mol. Phys. 102, 1057 (2004).
39. V. Guillerm et al., Angew. Chem. Int. Ed. 51, 9267 (2012).

Galvanic Replacement Reactions in Metal Oxide Nanocrystals

Myoung Hwan Oh,[1,2]* Taekyung Yu,[3]* Seung-Ho Yu,[1,2] Byungkwon Lim,[4] Kyung-Tae Ko,[5] Marc-Georg Willinger,[6] Dong-Hwa Seo,[7] Byung Hyo Kim,[1,2] Min Gee Cho,[1,2] Jae-Hoon Park,[5,8] Kisuk Kang,[7] Yung-Eun Sung,[1,2] Nicola Pinna,[2,9,10]† Taeghwan Hyeon[1,2]†

Galvanic replacement reactions provide a simple and versatile route for producing hollow nanostructures with controllable pore structures and compositions. However, these reactions have previously been limited to the chemical transformation of metallic nanostructures. We demonstrated galvanic replacement reactions in metal oxide nanocrystals as well. When manganese oxide (Mn_3O_4) nanocrystals were reacted with iron(II) perchlorate, hollow box-shaped nanocrystals of Mn_3O_4/γ-Fe_2O_3 ("nanoboxes") were produced. These nanoboxes ultimately transformed into hollow cagelike nanocrystals of γ-Fe_2O_3 ("nanocages"). Because of their nonequilibrium compositions and hollow structures, these nanoboxes and nanocages exhibited good performance as anode materials for lithium ion batteries. The generality of this approach was demonstrated with other metal pairs, including Co_3O_4/SnO_2 and Mn_3O_4/SnO_2.

The galvanic replacement reaction is the most versatile method of preparing hollow metallic nanostructures with controllable pore structures and compositions (1–7). These reactions involve a corrosion process that is driven by the difference in the electrochemical potentials of two metallic species. The hollow interior is generated from the oxidative dissolution of the metal nanocrystals (NCs) that are used as reactive templates. This strategy has also been used for the production of hollow semiconductor nanostructures (8). However, the chemical transformation of ionic systems via galvanic reactions has remained elusive. We demonstrated that a galvanic replacement reaction can occur in oxide NCs as well and can produce hollow oxide nanostructures.

Hollow oxide NCs have attracted much interest because of their potential for application in energy storage, catalysis, and medicine (9, 10). Considerable advances have been made in the synthesis of hollow oxide and semiconductor NCs (11–13). The Kirkendall effect has been exploited to produce complex hollow nanostructures of metal oxides and chalcogenides (11, 14–16). However, synthesizing hollow NCs of multimetallic oxides still remains a substantial challenge (17, 18). We showed that by using a nanoscale galvanic replacement reaction, monometallic oxide NCs could be completely transformed into hollow multimetallic oxide nanostructures. Contrary to what occurs in metallic systems, a redox-couple reaction between multivalent metallic ions